Electronic Structure and Charge Transport in Nanostripped Graphene

J. X. Lian,*,[†] A. Lherbier,[‡] L. J. Wang,[¶] J.-C. Charlier,[‡] D. Beljonne,[†] and Y. Olivier*,[†]

[†]Laboratory for Chemistry of Novel Materials, Université de Mons, Place du Parc 20, 7000 Mons, Belgium

[‡]Institute of Condensed Matter and Nanosciences, Université catholique de Louvain, Chemin des étoiles 8, 1348 Louvain-la-Neuve, Belgium

[¶]Department of Chemistry, Zhejiang University, Hangzhou 310027, China

Ⓢ Supporting Information

ABSTRACT: An attractive strategy to generate semiconducting graphene layers is delineating rows of sp^3 defects along the armchair direction that disrupt the π-conjugation and result in the formation of nanostripped structures with tunable band gap. This is investigated here using density functional theory (DFT) calculations, where we have assessed how much the electronic structure of the nanostructured graphene layers is affected by the density and structure of sp^3 defects. A parametrized tight-binding model is then mapped onto the DFT results, thereby allowing for extending the calculations to much larger system sizes (up to 10^6 atoms). We have next applied the real-space Kubo−Greenwood formalism to investigate the charge transport characteristics in graphene with various percentages of sp^3 defects. The calculations show that although incomplete saturation of the sp^3 defects density lines leads to the appearance of localized states within the otherwise band gap, those states do not participate in electron transport along the system, which remains effectively confined in the so-created quasi-one-dimensional semiconducting channels.
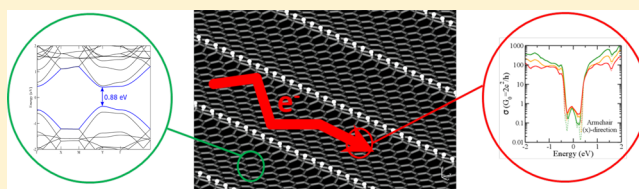
■ INTRODUCTION

Since its first experimental isolation in 2004, graphene has revealed outstanding physical and electronic properties,[1−3] which has opened new horizons to revolutionize nano-electronics and related integrated circuit techonologies.[4−6] In particular, experimental transport measurements show that graphene has remarkably high charge carrier mobility at room temperature,[1] with reported values of 200.000 $cm^2\,V^{-1}\,s^{-1}$, largely exceeding those reported for silicon.[7] However, due to its zero band gap, the potential of graphene in electronic applications is severely undermined.

Previous investigations on graphene nanoribbons (GNRs) have shown that their electronic and magnetic properties can be tuned by appropriate chemical design of the edges topology, inducing a semiconducting behavior[8−11] as well as a spin-polarized transport.[12,13] Armchair graphene nanoribbons (AGNRs) appear as an especially viable and promising route to provide GNR with semiconducting properties.[8] Indeed, the quantum confinement allows for the opening of an energy gap in graphene electronic structure, which scales inversely with the ribbon width.[9,10,14] It has been predicted that to produce materials with band gaps $E_g = 0.7$ eV, the width of the ribbons must be in the range of 2−3 nm.[15] However, the top-down approaches proposed so far to synthesize GNRs suffer from severe limitations related to the poor resolution, the reproducibility of the experiments, and the lack of control over the graphene edges.[16−27]

Physisorption on graphene introduces defect states around the Fermi level but can hardly open a band gap.[28] In contrast, the formation of covalent bonds converts the sp^2 carbons of graphene into sp^3 carbons, thereby locally opening a band gap in the electronic structure and generating semiconducting regions.[29,30] This approach has been successfully applied to other carbon nanostructures such as carbon nanotubes (CNTs).[31,32] Recently, random functionalization of graphene with phenyl diazonium salts has been demonstrated using an electrochemical approach, and a high conversion rate was achieved as probed by the intensity ratio between the D peak and G peak, I_D/I_G, in Raman spectra.[30] However, the chemisorption sites are relatively random, offering a very limited control of the functionalization pattern. Recent studies have shown that hydrogenation of the graphene surface is a promising yet simple way to tune graphene electronic properties.[33−39] Namely, it was predicted that the chemisorption of hydrogen atoms alternated on both sides of graphene surface leads to insulating behavior with a direct band gap of $E_g \sim 3.5$ eV.[40] This two-dimensional hydrocarbon material, the so-called *graphane*, is fully saturated with sp^3 hybridized carbon atoms and can be used to create an insulating phase in the graphene network.[41]

In this work, we study AGNRs engineered via alignment of hydrogen atoms bonded to carbon atoms forming sp^3 defects that disrupt the π-delocalization. Such an alignment of the sp^3 defects is expected to trigger the opening of a band gap while

keeping high charge carrier mobility, as required for field-effect transistors applications. Our first objective is to evaluate the influence of the periodic sp^3 defects on the electronic structure of the chemically modified graphene surfaces. The geometric structure of a stripped graphene system (SGS) delineated with sp^3 defects is shown in Figure 1. The hydrogen atoms (shown
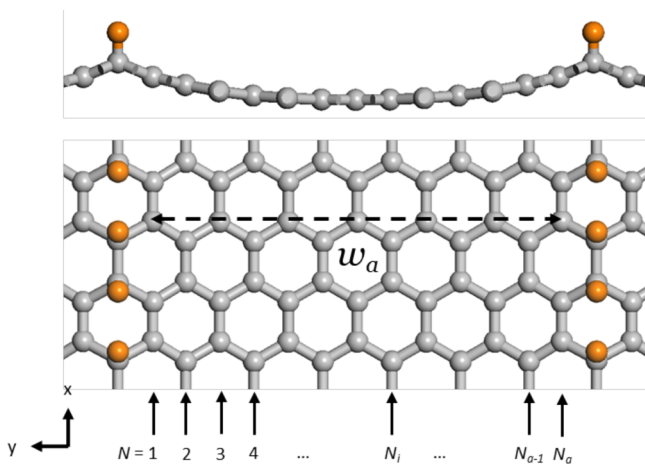

Figure 1. Schematic representation of a N_a-SGS. The orange atoms denote hydrogen atoms covalently bonded to the carbon atoms (light gray). The SGS width is represented by w_a and the ith carbon armchair dimer-line (along the x direction) is denoted by N_i.

in orange) are connected to carbon atoms of the graphene underneath (in gray), forming lines parallel to the armchair direction of graphene. The width is measured by the number of pristine sp^2-carbon dimer-lines (N_a) between the hydrogen lines. The dependence of the electronic structure with the ribbon width, density, and shape of the hydrogen lines is investigated by means of density functional theory (DFT) and a tight-binding (TB) model mapped onto the DFT calculations. Some leading quantum transport investigations on GNR-based systems have been reported previously, including Boltzmann model,[42−47] TB calculations,[47−49] and nonequilibrium Green functions.[49−51] Here, we have performed wave packet propagation simulations which allow for extracting the transport properties, namely the charge carrier mobility and elastic mean free path, obtained in the Kubo−Greenwood formalism.[52,53]

■ RESULTS AND DISCUSSION

First-Principles Electronic Structure. The calculations of the equilibrium ground-state geometries and the electronic band structure have been performed using DFT implementing periodic boundary conditions (PBC), with the Perdew−Burke−Ernzerhof exchange-correlation functional as implemented in Vienna Ab Initio Simulation Package (VASP). The projector augmented-wave pseudopentials were considered for ion−electron interaction. We used an energy cutoff of 400 eV to ensure the reliability of the results. The in-plane lattice parameters and atomic coordinates are optimized following the conjugate gradient scheme until the atomic forces are less than 0.02 eV Å^{-1}. Note that the unit cell axis normal to the SGS plane (z axis) is set to 30 Å to avoid any interaction between periodic cells. Convergence of the SCF cycle is reached when the energy difference between two steps is less than 10^{-7} eV. k-point samplings of $5 \times 3 \times 1$ and $21 \times 13 \times 1$ have been used

for geometric relaxation and electronic structure calculations, respectively.

Upon chemisorption of the hydrogen atoms on the graphene surface, the corresponding carbon atoms adopt a sp^3 hybridization and move out of the plane, leading to a buckling of the graphene sheet (Figure 1). We have addressed the lattice distortion in the Supporting Information, section S1. Figure 2
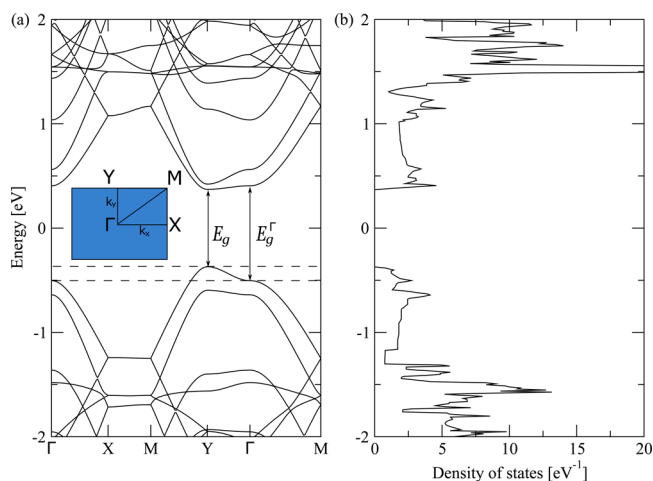

Figure 2. (a) Band structure and (b) density of states of 13-SGS (the Fermi level is set to zero). Band gaps E_g and E_g^Γ at Y and Γ, respectively, are shown by the arrows. The height between the two horizontal dashed lines delimiting the first valence band dispersion along the y axis is ∼0.12 eV. Inset: sketch of the first Brillouin zone and associated high-symmetry points.

features the electronic band structure and the associated density of states (DOS) as calculated for 13-SGS. The lattice parameters of the relaxed geometry are a = 12.9 Å and b = 17.1 Å, and the ribbon width is w_a = 14.6 Å. A fundamental direct band gap of E_g ∼ 0.74 eV is found at the Y high-symmetry point (see inset of Figure 2 left panel for a sketch of the Brillouin zone), while the band gap at Γ amounts to E_g^Γ ∼ 0.90 eV. The lines of hydrogen atoms generate parallel graphene pseudonanoribbons (aligned with the x axis), providing thus a one-dimensional (1D) character to the electronic structure. Indeed, it is observed that electronic dispersion along the y direction in reciprocal space (Γ−Y and X−M) is strongly reduced, which manifests itself by a rather flat valence band (VB) and conduction band (CB). The energies corresponding to these flat bands match those of van Hove singularities (DOS peaks), which again are signatures of the 1D character of the electronic structure. In contrast, there is a strong dispersion of VB and CB along the x axis, and the mobility of holes and electrons is thus expected to be reasonably high along that direction. Note that the dispersion of the first VB around Y is also quite non-negligible. Still, it rapidly flattens down at the Γ high-symmetry point, giving rise to only a small energy window (∼0.12 eV) of significant dispersion along the y direction. Conversely, the first CB along the Y−Γ branch appears to be rather flat; hence, an asymmetry in hole/electron conduction along the y axis is foreseen.

Not surprisingly, the electronic band gap is found to be quite sensitive to the degree of confinement. As the ratio of functionalized carbons decreases in the sp^3 defect lines, the band gap width is decreased (from 0.74 eV for a ratio of 100% to 0.30 and 0.10 eV at ratios of 66% and 50%, respectively), and

even disappears, reforming the Dirac point at low degree of functionalization, namely, 33% ratio (Figure 3). As expected, the band dispersion along X−M and Y−Γ is significantly increased, which suggests that charge transport might be significantly improved along the y direction.
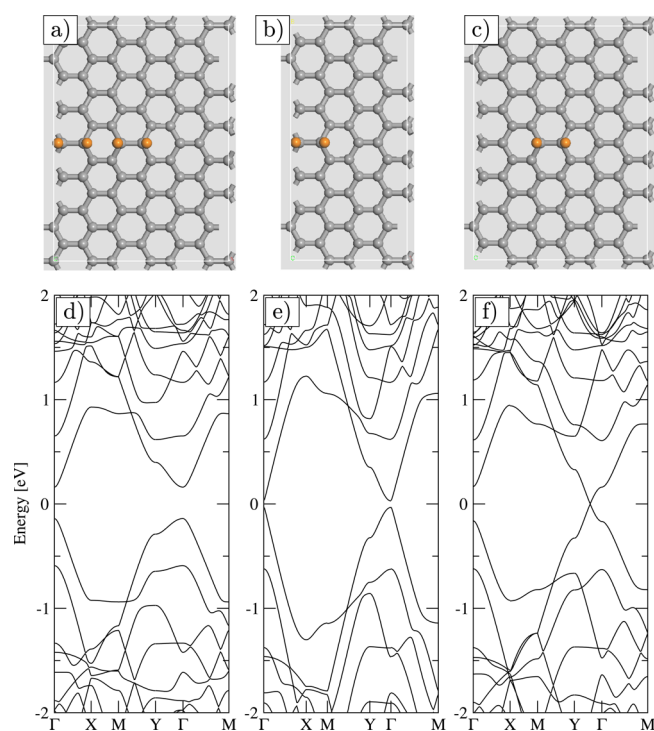

Figure 3. Geometric structures and electronic spectra of 13-SGS with 66% (a, d), 50% (b, e), and 33% (c, f) of hydrogenated carbon along the sp³ defect lines. The Fermi level is set to zero.

Similarly to the functionalization ratio, the degree of confinement is also affected by the functionalization pattern. In Figure 4, we report the electronic band structures of three systems that have the same amount of hydrogenated carbons in the lattice, namely, with six hydrogen atoms along the armchair direction of graphene. In contrast to the ideal structure where the hydrogen atoms are aligned along a single armchair carbon line, the following systems present different configurations of the hydrogen atoms along the defect line. In 13-SGS-meta, the hydrogen atoms are in meta position with respect to each other while they are arranged in ortho- or para-like configuration for the last two systems, labeled 13-SGS-ortho and 13-SGS-para, respectively. The 13-SGS-meta shows a relatively large band gap ($E_g \sim 1.5$ eV) with electronic states localized in the band gap region. These states originate from the symmetry breaking of the graphene lattice as only one sublattice of graphene is affected by the hydrogenation.[54,55] On the other hand, the symmetry is preserved in 13-SGS-ortho and 13-SGS-para, and no localized electronic states are found in the band gap region. The width of the energy gap in these nanostructures is lower than that of the perfectly aligned hydrogens 13-SGS. This can be explained by the lower degree of confinement in 13-SGS-ortho and 13-SGS-para. Interestingly, 13-SGS-ortho shows a relatively good dispersion of the first valence and conduction bands in the Y−Γ branch of the Brillouin zone. Thus, we can anticipate that both electrons and holes will be rather mobile along the direction perpendicular to the ribbon axis, as compared to 13-SGS-para.
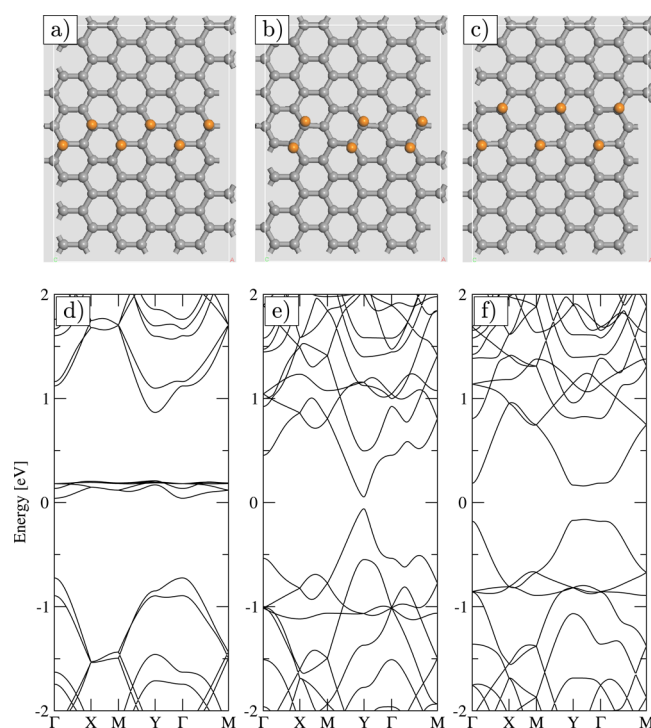

Figure 4. Geometric structures and electronic spectra of 13-SGS with hydrogen atoms in meta- (a,d), ortho- (b,e), and para- (c,f) positions in the sp³ defect lines. The Fermi level is set to zero.

The density of sp³ defects in these systems is identical to that with perfectly aligned hydrogenated carbons (i.e., 13-SGS), yet they show different relative stability. This is quantified here by comparing the binding energy per hydrogen atom, ΔE, defined as

$$E_{bind} = \frac{(E_{SGS} - E_0 - N_H \times E_H)}{N_H} \quad (1)$$

where E_{SGS} is the total energy of the SGS and E_0 and E_H are the total energies of the flat pristine graphene and of a single hydrogen atom, respectively. N_H is the number of hydrogen atoms in the SGS (six atoms in all cases). A negative value of ΔE indicates that the chemisorption of hydrogen atoms on graphene is energetically favorable (i.e., exergonic). In Table 1,

Table 1. Total Energy, E_{SGS} (Relative to Perfectly-Aligned Hydrogen, 13-SGS), and Binding Energy, E_{bind}, per Hydrogen Atom Calculated for Different Configurations of the sp³ Defects along the Armchair Direction of Graphene[a]

	E_{SGS} [eV]	E_{bind} [eV]
13-SGS	0	−1.75
13-SGS-meta	5.36	−0.86
13-SGS-ortho	2.13	−1.40
13-SGS-para	2.45	−1.34

[a]Additional data are given in the Supporting Information, section S1.

the relative total energies and binding energies per hydrogen atom are given (see Table S1 for the raw data). It is found that the 13-SGS has the lowest total energy, indicating that the alignment of the sp³ defects on a single carbon-dimer line is energetically more favorable. In contrast, chemisorption on a single sublattice of the graphene layer is less likely, as indicated by the relatively high energy in 13-SGS-meta. Interestingly, the

comparison between 13-SGS-ortho and 13-SGS-para indicates that the hydrogenation of carbon atoms that are covalently bonded is more favorable. This observation is in line with the expectation that the chemisorption of hydrogen atoms on the graphene surface creates a strong distortion of the lattice, which decreases the adsorption energy barrier on adjacent carbon sites and favors successive functionalization of graphene.[35]

We have estimated the effective mass of the charge carriers in 13-SGS and in the systems shown in Figures 3 and 4. The effective mass of holes and electrons are expressed in unit of electron mass (m_e) and are calculated from the valence band maximum (VBM) and conduction band minimum (CBM), respectively, both along armchair (m_{xx}^*) and zigzag (m_{yy}^*) directions. The results are reported in Table 2. Along the

Table 2. Predicted Band Gap, E_g, and Estimation of the Effective Mass (in Unit of Electron Mass) along Armchair (m_{xx}^*) and Zigzag (m_{yy}^*) Directions[a]

	E_g [eV]	carrier	m_{xx}^*	m_{yy}^*
13-SGS	0.74	h	0.24	0.61
		e	0.24	3.05
66%	0.30	h	0.17	1.22
		e	0.17	1.22
50%	0.06	h	0.15	0.41
		e	0.15	0.41
33%	0.00	h	0.00	0.00
		e	0.00	0.00
13-SGS-meta	1.59	h	0.41	1.22
		e	0.31	0.41
13-SGS-ortho	0.11	h	0.15	0.06
		e	0.15	0.06
13-SGS-para	0.32	h	0.24	2.03
		e	0.20	2.03

[a]The effective mass of the holes and electrons have been calculated from the valence band maximum (VBM) and the conduction band minimum (CBM), respectively, using the formula $m_{h,e}^* = \hbar^2/(\partial^2 E/\partial k^2)|_{VBM,CBM}$. In systems with decreasing functionalization ratio, VBM and CBM are symmetric and the predicted effective masses are the same for holes and electrons.

armchair direction (x axis), the effective masses of holes and electrons are identical in 13-SGS. This is expected from the symmetry between VB and CB along this direction ($\Gamma-X$ and $M-Y$ k-paths). In contrast, because VB exhibits some slight dispersion in the $Y-\Gamma$ region while the CB does not, a strong asymmetry of the effective mass between holes and electrons is thus predicted along the zigzag direction. As shown in the electronic band structure of the 13-SGS with decreasing functionalization ratio (see Figure 3), the band gap width decreases together with the effective mass. Especially, the 13-SGS with 33% functionalization ratio has zero energy gap and linear dispersion at the Fermi energy, which leads to the zero effective mass of the charge carriers. From this analysis, we expect the mobility to increase along the zigzag direction as the functionalization ratio is reduced and reaches values of pristine graphene in the limit of 0% functionalization ratio. When regarding the various patterns of the sp^3 defect line (Figure 4), the hole/electron effective mass changes, depending on the direction that is considered. As for systems with lower functionalization ratio, 13-SGS-ortho has a narrower energy gap and smaller effective mass for both directions (Figure 4b,e). In contrast, 13-SGS-para has rather flat valence and conduction

bands along the zigzag direction (y axis). Still, a slight dispersion is present in CB along the $Y-\Gamma$ path, which explains the smaller electron effective mass ($2.03 m_e$), compared to 13-SGS ($3.05 \, m_e$). On the other hand, the VB of 13-SGS in the $Y-\Gamma$ region is more dispersive than in 13-SGS-para, allowing for a smaller hole effective mass in 13-SGS. Along the armchair direction ($\Gamma-X$ and $M-Y$ regions), VB and CB are symmetric and the hole/electron effective mass is comparable to that in 13-SGS. Finally, the VBM and CBM in 13-SGS-meta are located at different high-symmetry points of the Brillouin zone, i.e. Γ and Y, respectively, and the asymmetry of VB and CB leads to the distinct but comparable effective masses between the holes and the electrons.

The electronic structure of hydrogen-aligned 13-SGS is compared to that of a 13-AGNR in Figure 5. There is a close
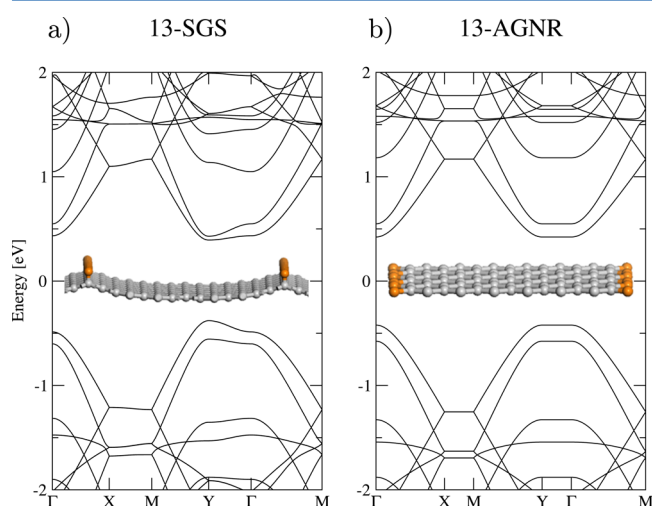
Figure 5. Geometric and electronic structures of (a) 13-SGS and (b) 13-AGNR. The Fermi level is set to zero.

similarity between the two band structure diagrams at the exception of the small dispersion of VB and CB along the $X-M$ and $Y-\Gamma$ branches for 13-SGS, as discussed above. These branches correspond to the transverse direction (across the H lines,) of the SGS, indicating the ability of holes and electrons to diffuse across the hydrogen lines, at least, in a narrow energy window. In addition, we have found that there is a close resemblance between the width-dependent energy gap of the SGS and the AGNR.[9] Indeed, the dependence of the energy gap with the SGS width can be distinguished into three semiconducting behaviors, i.e., with the number of carbon rows given by $3P$, $3P+1$, and $3P+2$ (where P is an integer).

The small dispersion observed along the $X-M$ and $Y-\Gamma$ branches is clearly related to the formation of Bloch waves due to the periodicity of the simulation box along the y direction. Such a dispersion most likely will be difficult to observe from an experimental point of view because a perfect atomic control on the width separating successive H lines is unlikely. To check this hypothesis, we have calculated the electronic structure of a 13-11-SGS superlattice in which we deliberately change the width of adjacent pseudoribbons, i.e., 13 and 11 carbon dimer lines are separated by hydrogen lines (Figure 6b). The electronic features of such a superlattice can be traced back to the electronic spectra of the constituting SGS, with slight differences. Indeed, the electronic bands of 13-SGS (Figure 6a) and those of 11-SGS (Figure 6c) are recognized in the close
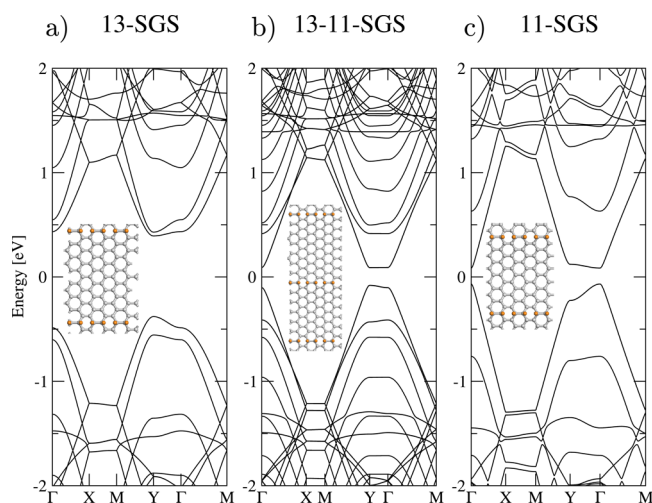
Figure 6. Geometric and electronic structures of (a) 13-SGS, (b) 13-11-SGS superlattice, and (c) 11-SGS. The Fermi level is set to zero.

Figure 7. 3NN-TB model. Carbon and hydrogen atoms are in gray and orange, respectively. On-site energy of "bulk" sp^2 carbon (blue ball), ϵ_{p_z}; on-site energy of sp^2 carbon next to sp^3 carbon (green balls), $\epsilon_{C1} = -3.388$ eV; on-site energy of sp^3 carbons (indicated by the red arrow and ball), $\epsilon_{CH} = 8$ eV; the transfer integrals (γ_1, γ_2, and γ_3) between first-, second-, and third-nearest neighbors are indicated by the red, green, and orange dashed lines, respectively.

spectrum of the superlattice, but they now appear much more flattened along the X−M and Y−Γ paths. This thus confirms that dispersion along the y axis, i.e., across the H lines, is strongly reduced in nanostripped graphene with finite distribution of pseudoribbon widths. Note also that the energy gap between the VB and CB of the 11-SGS is smaller than that of 13-SGS, although 11-SGS has a lower ribbon width ($w_a = 12.3$ Å). This is explained by the fact that the 11-SGS belongs to the $3P + 2$ family, while 13-SGS is a $3P + 1$ pseudoribbon.[9] Indeed, the calculated electronic band gaps are the lowest for the $3P + 2$ systems and the highest for the $3P + 1$ (see the Supporting Information, section S2), as found for the hydrogen-terminated AGNRs.

Tight-Binding Electronic Structure. On the basis of the first-principles electronic structures obtained previously, we have developed a third-nearest-neighbor tight-binding (3NN-TB) model (see Figure 7) within the orthogonal basis set approximation accounting for PBC. In our implementation of the 3NN-TB model, we proceeded in two steps: we first determined the TB parameters including the onsite energy ϵ_{p_z} (blue ball) and the three transfer integrals, γ_1, γ_2, and γ_3 (red, green, and orange dashed lines, respectively) by fitting the band structure of pristine graphene for different lattice constants, namely, $0.990a_0$, $0.995a_0$, a_0, $1.005a_0$, and $1.010a_0$, where a_0 is the equilibrium lattice constant in pristine graphene. Indeed, the chemisorption of the hydrogens on graphene is expected to distort the graphene lattice. We assume that the local deformation induced by the chemisorption affects the TB parameters similarly to a homogeneous crystal deformation, i.e., the graphene lattice was uniformly stretched by applying a change of the lattice constant.

The onsite energies have been aligned with the Fermi levels of pristine graphene at each lattice constant, while we tuned the transfer integrals so that the fitting of the CB and VB against the DFT results leads to the lowest mean square error. Finally, the onsite energy and the transfer integrals were adjusted considering an exponential dependence with the C−C bond length:

$$\epsilon_{p_z} = E_F - 4.782 + 12.204 \exp(-0.5783 \langle d_{CC} \rangle) \tag{2}$$
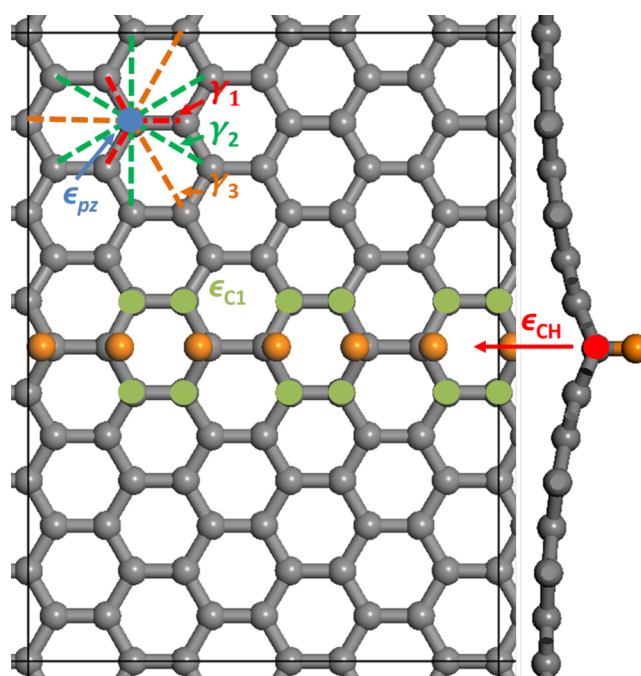
$$\gamma_1 = +1.426 + 475.6 \exp(-3.902 d_1) \tag{3}$$

$$\gamma_2 = -0.038 - 1816 \exp(-3.808 d_2) \tag{4}$$

$$\gamma_3 = +0.189 + 6515 \exp(-3.697 d_3) \tag{5}$$

where E_F is the Fermi level and $\langle d_{CC} \rangle$ is the average distance between one sp^2 carbon and its three first-nearest neighbors. For the hopping integrals, d_1, d_2, and d_3 are the distances between the sp^2 carbon and its first-, second-, and third-nearest neighbor, respectively. Note that the decaying exponentials provide lower standard error of estimate as compared to linear interpolation.[56]

In Figure 8, we report the band structure of a monoclinic 3×3-supercell of pristine graphene at lattice constants of $0.990a_0$, a_0, and $1.010a_0$, as calculated at the DFT level (black solid lines) and the 3NN-TB model (blue and pink circles, respectively). The 3NN-TB model is found to reproduce well the band structure of pristine graphene. Especially, the first CB is properly fitted in a wide range of wave vectors around the Γ point, which is an important prerequisite for a proper description of charge transport.[57]

Next, we modeled the chemisorption of hydrogen atoms on graphene, which leads to the rehybridization of the carbons from sp^2 to sp^3 (red ball in Figure 7). Similarly to graphene, it is assumed that the electronic properties of the SGS are governed by the π electrons. In this model, the hydrogen atoms are therefore not explicitly accounted for. Indeed, the onsite energies of the hydrogenated carbons are intentionally set at high energy value ($\epsilon_{CH} = 8$ eV) such that they produce decoupled eigenstates outside the π−π* spectrum of graphene. In addition, the transfer integrals between sp^2 atoms and sp^3 carbons are neglected. This means that dispersion across the H lines is mainly governed by second- and third-nearest sp^2
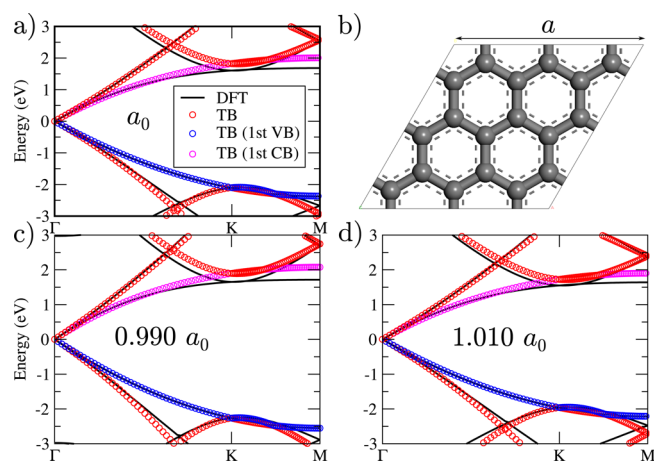
Figure 8. Mapping of the DFT bands (black solid lines) with 3NN-TB model (red circles) for a stretched monoclinic 3 × 3-supercell of pristine graphene (panel b) along Γ−K−M. The first valence and conduction bands from DFT calculations are fitted with the 3NN-TB model (blue and pink circles, respectively) within an energy window of 1 eV around the Fermi level (set to zero) and for lattice constants of (a) a_0, (c) $0.990a_0$, and (d) $1.010a_0$ where a_0 is the equilibrium lattice constant of the graphene supercell.

carbon neighbors on each side of the defect lines. Also, the sp^2 carbons that are connected to the sp^3 defects (called C1, green balls in Figure 7) are expected to undergo a perturbation that translates into a change of their onsite energies, ϵ_{C1}. Depending on the chemical environment of these C1 carbons (e.g., density of sp^3 defects, defect line pattern, etc.), the onsite parameter ϵ_{C1} was optimized so as to reproduce the DFT electronic band structures. For that purpose, an effective onsite energy has been calculated; i.e., $\epsilon_{C1} = -3.388$ eV. In Figure 9, we compare the
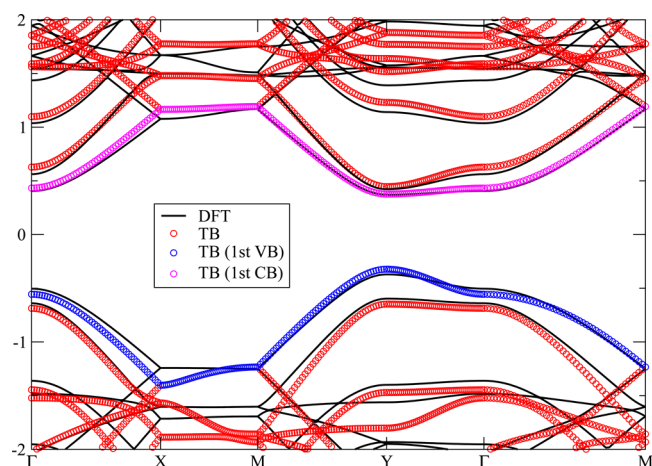

Figure 9. Mapping of the DFT bands (black solid lines) with 3NN-TB model (red circles) for 13-SGS along Γ−X−M−Y−Γ−M. The first valence and conduction bands from DFT calculations are fitted with the 3NN-TB model (blue and pink circles, respectively) within an energy window of 1 eV around the Fermi level (set to zero).

DFT band structure (black solid lines), and the 3NN-TB valence and conduction bands (blue and pink circles, respectively) of 13-SGS. Both VB and CB calculated with 3NN-TB model are in agreement with the DFT results over a wide range of wave vectors around the Γ point.

Quantum Transport Properties. Using the above-developed TB model, one can generate the electronic Hamiltonian for systems containing up to millions of atoms, approaching system sizes that are commensurate with graphene-based devices. Several 200 × 200 nm^2 graphene planes were thus created by repeating a 13-SGS rectangular unitcell in both planar directions.

We have investigated the impact on the shape of the DOS for different functionalization ratios, i.e., 90%, 80%, and 60% of sp^3 carbons in the hydrogenated carbons line. In these disordered graphene systems, 10%, 20%, and 40% of the hydrogen atoms, respectively, were randomly removed from the hydrogen lines. For the sake of comparison, the ideal case (100% functionalization ratio) was also considered. For such large systems, one cannot perform an exact diagonalization of the Hamiltonian. We thus resort to the Haydock recursion scheme to compute the DOS of such large disordered systems.[58] In Figure 10, we report the DOS of the ideal system obtained
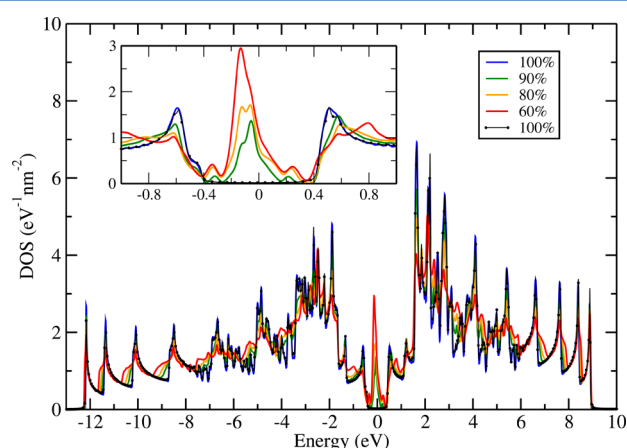

Figure 10. Density of states of the ideal 13-SGS (black dotted line and blue line) together with the density of states of 200 × 200 nm^2 planes with 90%, 80%, and 60% functionalization ratio of the H lines.

from both the recursion technique on a 200 × 200 nm^2 graphene sheet and an exact diagonalization of the 13-SGS, whose DFT counterpart was already shown in Figure 2.

Although the used recursion technique is not exact, one can clearly see that it captures very well all the DOS features of the ideal system when compared to the results obtained by exact diagonalization (blue solid line and black dotted line in Figure 10, respectively). As the functionalization ratio is decreased from 100%, one notices the appearance of a peak in the otherwise band gap region. The height of this peak increases with the amount of disorder; it is actually composed of a main central peak with two satellite peaks on each side (see magnified view in the inset of Figure 10). The states associated with this DOS peak are states localized around the defects. Such states can be related with the band edge states observed in Figure 3. One also notices that the van Hove singularities (VHS) are smoothened by the disorder. Overall, apart from the appearance of a peak in the band gap and the smoothening of VHS, the 1D character of the disordered systems remains clearly visible.

Using a real-space order-*N* Kubo−Greenwood method,[59−61] the transport properties of large graphene planes functionalized with H lines discussed above were predicted in both *x* and *y*

directions, i.e. parallel and perpendicular to the H lines, respectively.

The transport properties are inferred from the time propagation of random-phase wave packets. The propagation of wave packets is computed through the time-dependent Schrödinger equation by solving the time-evolution operator $\hat{U}(t) = \exp(-i\hat{H}t/\hbar)$ with an efficient Chebyshev polynomial method. It allows for computing time and energy-dependent mean quadratic spreading along each direction ($\Delta\hat{X}^2(E,t)$ and $\Delta\hat{Y}^2(E,t)$, $\hat{X}$ and $\hat{Y}$ being the quantum position operator). The diffusivity in a given direction is then evaluated directly from this quadratic spreading. For instance along the x direction one has $D_x(E,t) = \Delta\hat{X}^2(E,t)/t$ with $\Delta\hat{X}^2(E,t) = \text{Tr}[\delta(E - \hat{H})|\hat{X}(t) - \hat{X}(0)|^2]/\text{Tr}[\delta(E - \hat{H})]$ and with $\hat{X}(t) = \hat{U}(t)^\dagger\hat{X}(0)\hat{U}(t)$. Within the semiclassical picture, the diffusivity either increases linearly with time and infinitely in the ballistic limit when no scattering occurs or (as found here) increases and then saturates to a maximal value, D_{max}, in the thermodynamic limit, i.e., after a large number of scattering events. The elastic mean free path, l_e; the conductivity, σ; and the mobility, μ, discussed in the following are semiclassical quantities deduced from the maximum of diffusivity curves (D^{max}) as $l_e = D^{max}/2v$ where v is the carrier velocity, $\sigma^{sc} = e^2\rho D^{max}/2$ where e is the elementary charge and ρ is the density of states per surface area, and $\mu = \sigma/ne$ where n is the charge carrier density.

The elastic mean free path is found to be extremely short (most of the times lower than ~5 nm) in the y direction (right panel in Figure 11), except around the charge carrier energy E
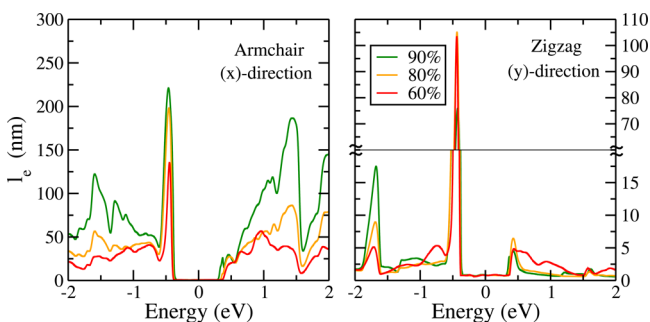

Figure 11. Charge carrier mean free paths in both x and y principal directions.

= −0.45 eV, where it reaches a value of 100 nm. This energy corresponds to the first VB for which a significant dispersion is observed (see the region delimited by the dashed lines in Figure 2) confirming the previous analysis performed on the band structure. In the x direction, the mean free path is predicted to be in the range [20−200] nm depending on the charge carrier energy and on the averaged defect density. The mean free path is found to globally decrease with decreasing functionalization ratio. A peak is observed at the onset of the first VB (E = −0.45 eV) similarly to the y direction. Such pronounced peaks in the mean free path (Figure 11) are concomitant with the existence of a single band transport.[62,63] Indeed, in the presence of only one electronic band, scattering possibilities are strongly reduced compared to situations with two or many bands coexisting at the same energy, which is the case for CB. Finally and most importantly, we observe in all cases the formation of a clear transport gap of approximately 0.7 eV (~E_g), while a pronounced peak in the DOS (Figure 10) indicates the presence of electronic states close to the Fermi

energy. Hence, the transport gap confirms that those states are localized and do not participate to the transport, so that the semiconducting properties of the disordered pseudonanoribbons are preserved.

The charge carrier mobility (μ) computed from the quadratic spreading and for a given Fermi−Dirac distribution determined at a temperature of 300 K is presented in Figure 12. Because
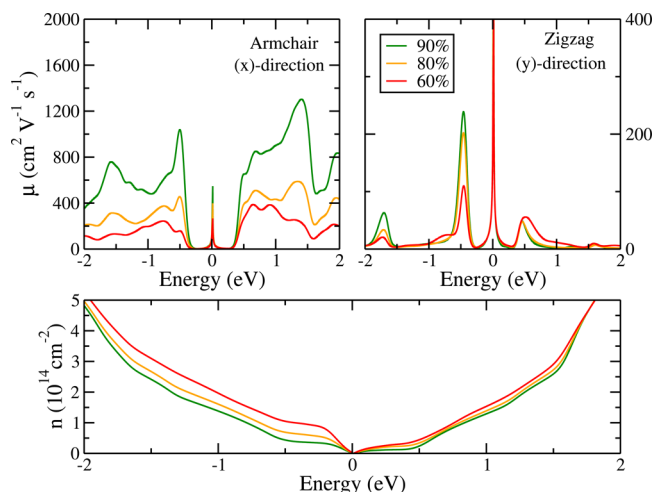

Figure 12. Charge carrier mobility in both x and y principal directions together with charge carrier density.

the mobility is inversely proportional to the charge carrier density (n), it diverges at the equilibrium Fermi energy (E_F^0) which was positioned at E = 0 eV (center of the gap), where n = 0 cm^{-2} (see lower panel of Figure 12). This mathematical divergence is clearly observed in mobility curves in Figure 12 but has no physical meaning as in real devices the charge density hardly approaches zero, thus washing out such a divergence. Similarly to the mean free path, μ is found to be almost zero in the y direction (except for the onset of the first VB) while it is in the range ~[200−2000] cm^2 V^{-1} s^{-1} in the x direction. As discussed in the case of the 13-11-SGS superlattice, the dispersion of VB along the y direction is an artifact of the perfect periodicity and is therefore unexpected in real experimental conditions. The calculated semiclassical conductivity, σ^{sc}, is depicted in Figure 13 for two different Fermi−Dirac temperatures of 300 and 100 K (solid and dashed lines, respectively). Again, one distinguishes the remnants of a transport gap. However, the presence of localized states in the gap prevents the efficient turning off of the current in this gap.
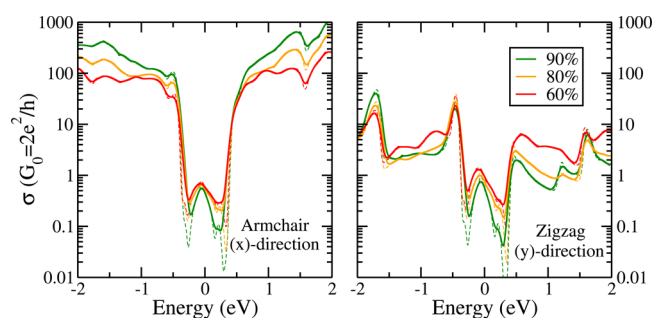

Figure 13. Semiclassical conductivity in both x and y principal directions (left and right panels, respectively) at Fermi−Dirac temperatures of 300 and 100 K (solid and dashed lines, respectively).

Nevertheless, an on/off ratio of the order of 10^3 is predicted. The calculated transport properties confirm the semiconducting and the 1D character of the system, which is found to be robust against disorder even down to a 60% functionalization ratio.

Compared to the situation observed in First-Principles Electronic Structure section, which discussed the case of periodic small supercells whose band structure reveals the closing of the band gap for decreasing functionalization ratio (Figure 3), the present situation with a more realistic disordered distribution of hydrogen atoms shows that the transport gap remains almost equivalent to the band gap computed for the ideal case of 100% functionalization ratio. The presence of states within the gap is induced by the formation of local patterns as discussed previously (see also Figure 3). However, their random distribution avoids the formation of extended Bloch states, creating instead localized states which do not participate efficiently to transport. Finally, one can anticipate that the system will slowly recover a fully two-dimensional (2D) character by further decreasing the functionalization ratio down to the limit of perfect graphene. In particular, the DOS of such low functionalization ratio should look like the well-known DOS of pristine graphene with a V-shape close to the Dirac point region. Obviously from Figure 10, the 60% functionalization case is still far from this 2D graphene situation.

CONCLUSIONS

To conclude, we have shown, as a proof of concept, that graphene systems delineated with chemisorbed hydrogen atoms, playing the role of sp^3 defects, have electronic properties comparable with respect to conventional AGNRs. The electronic and transport properties of the SGS are highly sensitive to the detailed shape of the hydrogen lines and to the degree of functionalization of the graphene surface. The ratio of hydrogenated carbons over sp^2 carbons along the armchair line, as well as the functionalization pattern, have been varied while simultaneously probing the electronic structure of the SGS. We have adopted a multiscale approach combining DFT calculations and tight-binding model for the generation of electronic structures of realistic graphene systems. Using the real-space order-N Kubo−Greenwood formalism, we have shown that the confinement provided by these hydrogenated carbons is important in order to efficiently limit the charge transport in one direction. Deviation from the fully hydrogenated carbon lines gives rise to the appearance of localized defect states within the band gap, which leads to scattering of the charge carriers. The theoretical results presented here are encouraging in two different respects. First, we found that the opening of a band gap in the graphene electronic structure upon formation of sp^3 defect lines shows a high tolerance with respect to the positioning and density of the defects. In addition, high (low) charge carrier mobility values are predicted in resonance with the semiconducting states ∼0.5 eV away from (around) the Fermi energy, thus sustaining high on/off current ratios.

ASSOCIATED CONTENT

Ⓢ Supporting Information

The Supporting Information is available free of charge on the ACS Publications website at DOI: 10.1021/acs.jpcc.6b06265.

Discussion of the lattice distortion, i.e., $(E − a,b)$ relation, of graphene upon chemisorption of H atoms; details regarding the width-dependent energy gap (PDF)

AUTHOR INFORMATION

Corresponding Authors

*E-mail: jian.lian@umons.ac.be.
*E-mail: yoann.olivier@umons.ac.be.

Notes

The authors declare no competing financial interest.

REFERENCES

(1) Geim, A. K.; Novoselov, K. S.; Morozov, S. V.; Jiang, D.; Zhang, Y.; Dubonos, S. V.; Grigorieva, I. V.; Firsov, A. A. *Science* **2004**, *306*, 666−669.

(2) Geim, A. K.; Novoselov, K. S. *Nat. Mater.* **2007**, *6*, 183−191.

(3) Falko, V. I.; Geim, A. K. *Eur. Phys. J.: Spec. Top.* **2007**, *148*, 1−4.

(4) Schwierz, F. *Nat. Nanotechnol.* **2010**, *5*, 487−496.

(5) Bae, S.; Kim, S. J.; Shin, D.; Ahn, J.-H.; Hong, B. H. *Phys. Scr.* **2012**, *T146*, 014024.

(6) Terrones, M.; Botello-Méndez, A. R.; Campos-Delgado, J.; López-Urías, F.; Vega-Cantú, Y. I.; Rodríguez-Macías, F. J.; Elías, A. L.; Muñoz Sandoval, E.; Cano-Márquez, A. G.; Charlier, J.-C.; Terrones, H. *Nano Today* **2010**, *5*, 351−372.

(7) Morozov, S. V.; Novoselov, K. S.; Katsnelson, M. I.; Schedin, F.; Elias, D. C.; Jaszczak, J. A.; Geim, A. K. *Phys. Rev. Lett.* **2008**, *100*, 016602.

(8) Dubois, S.-M.; Zanolli, Z.; Declerck, X.; Charlier, J.-C. *Eur. Phys. J. B* **2009**, *72*, 1−28.

(9) Son, Y.-W.; Cohen, M. L.; Louie, S. G. *Phys. Rev. Lett.* **2006**, *97*, 216803.

(10) White, C. T.; Li, J.; Gunlycke, D.; Mintmire, J. W. *Nano Lett.* **2007**, *7*, 825−830.

(11) Chen, L. P.; Wang, L. J.; Beljonne, D. *Carbon* **2014**, *77*, 868−879.

(12) Fujita, M.; Wakabayashi, K.; Nakada, K.; Kusakabe, K. *J. Phys. Soc. Jpn.* **1996**, *65*, 1920−1923.

(13) Muñoz Rojas, F.; Fernández-Rossier, J.; Palacios, J. J. *Phys. Rev. Lett.* **2009**, *102*, 136810.

(14) Long, L.; Tang, M. Q.; Wang, D.; Wang, L. J.; Shuai, Z. *J. Am. Chem. Soc.* **2009**, *131*, 17728−17729.

(15) Barone, V.; Hod, O.; Scuseria, G. E. *Nano Lett.* **2006**, *6*, 2748−2754.

(16) Han, M. Y.; Ozyilmaz, B.; Zhang, Y.; Kim, P. *Phys. Rev. Lett.* **2007**, *98*, 206805.

(17) Chen, Z. H.; Lin, Y. M.; Rooks, M. J.; Avouris, P. *Phys. E* **2007**, *40*, 228−232.

(18) Wu, Z. S.; Ren, W.; Gao, L.; Liu, B.; Zhao, J.; Cheng, H. M. *Nano Res.* **2010**, *3*, 16−22.

(19) Tapasztó, L.; Dobrik, G.; Lambin, P.; Biró, L. P. *Nat. Nanotechnol.* **2008**, *3*, 397−401.

(20) Wang, X.; Dai, H. *Nat. Chem.* **2010**, *2*, 661−665.

(21) Jiao, L.; Zhang, L.; Wang, X.; Diankov, G.; Dai, H. *Nature* **2009**, *458*, 877−880.

(22) Kosynkin, D. V.; Higginbotham, A. L.; Sinitskii, A.; Lomeda, J. R.; Dimiev, A.; Price, B. K.; Tour, J. M. *Nature* **2009**, *458*, 872−876.

(23) Elías, A. L.; Botello-Méndez, A. R.; Meneses-Rodríguez, D.; González, V. J.; Ramírez-González, D.; Ci, L.; Muñoz Sandoval, E.; Ajayan, P. M.; Terrones, H.; Terrones, M. *Nano Lett.* **2010**, *10*, 366−372.

(24) Jiao, L.; Wang, X.; Diankov, G.; Wang, H.; Dai, H. *Nat. Nanotechnol.* **2010**, *5*, 321−325.

(25) Campos-Delgado, J.; et al. *Nano Lett.* **2008**, *8*, 2773−2778.

(26) Wei, D.; Liu, Y.; Zhang, H.; Huang, L.; Wu, B.; Chen, J.; Yu, G. *J. Am. Chem. Soc.* **2009**, *131*, 11147−11154.

(27) Ma, L.; Wang, J.; Ding, F. *ChemPhysChem* **2013**, *14*, 47−54.

(28) Chen, L. P.; Wang, L. J.; Shuai, Z.; Beljonne, D. *J. Phys. Chem. Lett.* **2013**, *4*, 2158−2165.

(29) Quintana, M.; Grzelczak, M.; Prato, M. *Phys. Status Solidi B* **2010**, *247*, 2645−2648.

(30) Shih, C.-J.; Wang, Q. H.; Jin, Z.; Paulus, G. L. C.; Blankschtein, D.; Jarillo-Herrero, P.; Strano, M. S. *Nano Lett.* **2013**, *13*, 809−817.

(31) Singh, P.; Campidelli, S.; Giordani, S.; Bonifazi, D.; Bianco, A.; Prato, M. *Chem. Soc. Rev.* **2009**, *38*, 2214−2230.

(32) Ménard-Moyon, C.; Izard, N.; Doris, E.; Mioskowski, C. *J. Am. Chem. Soc.* **2006**, *128*, 6552−6553.

(33) Casolo, S.; Løvvik, O. M.; Martinazzo, R.; Tantardini, G. F. *J. Chem. Phys.* **2009**, *130*, 054704.

(34) Chernozatonskii, L. A.; Sorokin, P. B.; Brüning, J. W. *Appl. Phys. Lett.* **2007**, *91*, 183103.

(35) Stojkovic, D.; Zhang, P.; Lammert, P. E.; Crespi, V. H. *Phys. Rev. B: Condens. Matter Mater. Phys.* **2003**, *68*, 195406.

(36) Denis, A. P.; Iribarne, F. *J. Mol. Struct.: THEOCHEM* **2009**, *907*, 93−103.

(37) Hornekær, L.; Šljivančanin, Ž.; Xu, W.; Otero, R.; Rauls, E.; Stensgaard, I.; Laegsgaard, E.; Hammer, B.; Besenbacher, F. *Phys. Rev. Lett.* **2006**, *96*, 156104.

(38) Mirzadeh, M.; Farjam, M. *J. Phys.: Condens. Matter* **2012**, *24*, 235304.

(39) Nilsson, L.; Šljivančanin, Ž.; Balog, R.; Xu, W.; Linderoth, T. R.; Lægsgaard, E.; Stensgaard, I.; Hammer, B.; Besenbacher, F.; Hornekær, L. *Carbon* **2012**, *50*, 2052−2060.

(40) Sofo, J. O.; Chaudhari, A. S.; Barber, G. D. *Phys. Rev. B: Condens. Matter Mater. Phys.* **2007**, *75*, 153401.

(41) Singh, A. K.; Yakobson, B. I. *Nano Lett.* **2009**, *9*, 1540−1543.

(42) Long, M.; Tang, L.; Wang, D.; Wang, L.; Shuai, Z. *J. Am. Chem. Soc.* **2009**, *131*, 17728−17729.

(43) Bruzzone, S.; Fiori, G. *Appl. Phys. Lett.* **2011**, *99*, 222108.

(44) Xi, J.; Long, M.; Tang, L.; Wang, D.; Shuai, Z. *Nanoscale* **2012**, *4*, 4348−4369.

(45) Wang, J.; Zhao, R.; Yang, M.; Liu, Z.; Liu, Z. *J. Chem. Phys.* **2013**, *138*, 084701.

(46) Chen, L.; Wang, L.; Beljonne, D. *Carbon* **2014**, *77*, 868−879.

(47) Klos, J. W.; Zozoulenko, I. V. *Phys. Rev. B: Condens. Matter Mater. Phys.* **2010**, *82*, 081414.

(48) Gunlycke, D.; Vasudevan, S.; White, C. T. *Nano Lett.* **2013**, *13*, 259−263.

(49) Chin, S.-K.; Lam, K.-T.; Seah, D.; Liang, G. *Nano. Res. Lett.* 20, *7*, 114.

(50) Kim, W. Y.; Kim, K. S. *Nat. Nanotechnol.* **2008**, *3*, 408−412.

(51) Min, S. K.; Kim, W. Y.; Cho, Y.; Kim, K. S. *Nat. Nanotechnol.* **2011**, *6*, 162−165.

(52) Lherbier, A.; Dubois, S. M.-M.; Declerck, X.; Niquet, Y.-M.; Roche, S.; Charlier, J.-C. *Phys. Rev. B: Condens. Matter Mater. Phys.* **2012**, *86*, 075402.

(53) Lherbier, A.; Roche, S.; Restrepo, O. A.; Niquet, Y.-M.; Delcorte, A.; Charlier, J.-C. *Nano Res.* **2013**, *6*, 326−334.

(54) Pereira, V. M.; Guinea, F.; Lopes dos Santos, J. M. B.; Peres, N. M. R.; Castro Neto, A. H. *Phys. Rev. Lett.* **2006**, *96*, 036801.

(55) Pereira, V. M.; Lopes dos Santos, J. M. B.; Castro Neto, A. H. *Phys. Rev. B: Condens. Matter Mater. Phys.* **2008**, *77*, 115109.

(56) Wohlthat, S.; Reimers, J. R.; Hush, N. S. *Phys. Rev. B: Condens. Matter Mater. Phys.* **2010**, *81*, 195125.

(57) Reich, S.; Maultzsch, J.; Thomsen, C.; Ordejón, P. *Phys. Rev. B: Condens. Matter Mater. Phys.* **2002**, *66*, 035412.

(58) Haydock, R. *Solid State Phys.* **1980**, *35*, 215−294.

(59) Mayou, D.; Khanna, S. N. *J. Phys. I* **1995**, *5*, 1199−1211.

(60) Triozon, F.; Vidal, J.; Mosseri, R.; Mayou, D. *Phys. Rev. B: Condens. Matter Mater. Phys.* **2002**, *65*, 220202.

(61) Lherbier, A.; Dubois, S.-M.; Declerck, X.; Niquet, Y.-M.; Roche, S.; Charlier, J.-C. *Phys. Rev. B: Condens. Matter Mater. Phys.* **2012**, *86*, 075402.

(62) Lherbier, A.; Persson, M. P.; Niquet, Y.-M.; Triozon, F.; Roche, S. *Phys. Rev. B: Condens. Matter Mater. Phys.* **2008**, *77*, 085301.

(63) Persson, M. P.; Lherbier, A.; Niquet, Y.-M.; Triozon, F.; Roche, S. *Nano Lett.* **2008**, *8*, 4146−4150.